
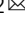




## Towards entanglement distillation between atomic ensembles using high-fidelity spin operations

Chao Liu <sup>1,2</sup>, Tao Tu <sup>1,2</sup>✉, Pei-Yun Li<sup>1,2</sup>, Xiao Liu<sup>1,2</sup>, Xing-Yu Zhu<sup>1,2</sup>, Zong-Quan Zhou <sup>1,2</sup>✉, Chuan-Feng Li <sup>1,2</sup>✉ & Guang-Can Guo<sup>1,2</sup>

Entanglement distillation is an essential ingredient for long-distance quantum communication. However, owing to their demanding requirements, integrating such entanglement distillation processing in scalable quantum devices remains an outstanding challenge. Here we propose the implementation of the filtering protocol in atomic ensembles, which are promising candidates for building quantum repeater nodes, and analyze the boost entanglement distribution rate considering different scenarios. Moreover, we demonstrate the key step of this approach with a proof-of-principle experiment in a rare-earth-ion-doped crystal ( $^{143}\text{Nd}^{3+}:\text{Y}_2\text{SiO}_5$ ). Leveraging its multi-level structure and long-lived coherence, spin manipulations are implemented with an average fidelity exceeding 97.2%, leading to the preparation of entanglement between the electron and nuclear spins with a concurrence of 0.75 with a sample temperature of 100 mK. The versatility, robustness, and potential scalability of our proposal contribute to the construction of quantum repeaters and quantum networks based on atomic ensembles.

<sup>1</sup>CAS Key Laboratory of Quantum Information, University of Science and Technology of China, Hefei 230026, China. <sup>2</sup>CAS Center for Excellence in Quantum Information and Quantum Physics, University of Science and Technology of China, Hefei 230026, China. ✉email: [tutao@ustc.edu.cn](mailto:tutao@ustc.edu.cn); [zq\\_zhou@ustc.edu.cn](mailto:zq_zhou@ustc.edu.cn); [cfl@ustc.edu.cn](mailto:cfl@ustc.edu.cn)

Entanglement between spatially separated nodes is a unique resource for an array of quantum information applications including secure quantum communication<sup>1–3</sup>, distributed quantum computation<sup>4</sup>, and enhanced metrology<sup>5–7</sup>. Such capabilities fundamentally depend on the quality of the entanglement between distant nodes. Therefore, it is a key task to generate and manipulate the remote entanglement with high fidelity in the presence of various errors and imperfections. To address this problem, various entanglement purification (or distillation) protocols have been developed<sup>8–11</sup>. Entanglement purification has been successfully demonstrated based on entangled photon pairs in a series of experiments<sup>12–14</sup>. However, the purified entangled photon pairs are unavoidably lost upon the success of the purification procedures due to the lack of quantum memories, preventing them from being further exploited. Non-destructive entanglement purification is carried out using single N-V centers<sup>15</sup> and single atoms<sup>16</sup>, in which the purified entangled states are stored for further use, such as

conducting the entanglement purification procedure of the next round or the entanglement swapping procedure between neighboring nodes.

The atomic ensembles are promising candidates for quantum repeaters and quantum networks<sup>17</sup>, thanks to the collective enhancement between many atoms which results into high collection efficiency for signal photons<sup>18</sup>. Remarkable progresses have been made on the realization of quantum repeaters and quantum communication on the basis of the atomic ensembles<sup>17–22</sup>. However, there has been no demonstration of entanglement purification of discrete variables on atomic ensembles so far, since the purification protocols usually require the complex combination of high-fidelity quantum gates, long-term quantum storage, high-efficiency detection, or non-demolition qubit readout<sup>15,23,24</sup>, which are still challenging to be implemented on atomic ensembles.

Here, we propose the application of the filtering protocol<sup>25,26</sup> using a single copy of two-qubits entangled state in atomic ensembles to gain increased fidelity. The present proposal is based on local operations (LOs) and detection on the spin states of the atomic ensembles in each node. We further illustrate that the entanglement connection (EC) process can be improved by combining these LOs and detection. As a proof-of-principle demonstration, we implement these elementary LOs on the hybrid electron-nuclear spins in a <sup>143</sup>Nd<sup>3+</sup>:Y<sub>2</sub>SiO<sub>5</sub> crystal, which is a promising material for quantum repeater nodes<sup>27–30</sup>. The combination of these high-quality LOs generates an entangled state between the electron spins and nuclear spins with a concurrence of 0.75 and a fidelity of 92.8% compared with the Bell state. These results provide useful tools toward the construction of large-scale quantum networks based on the solid-state atomic ensembles.

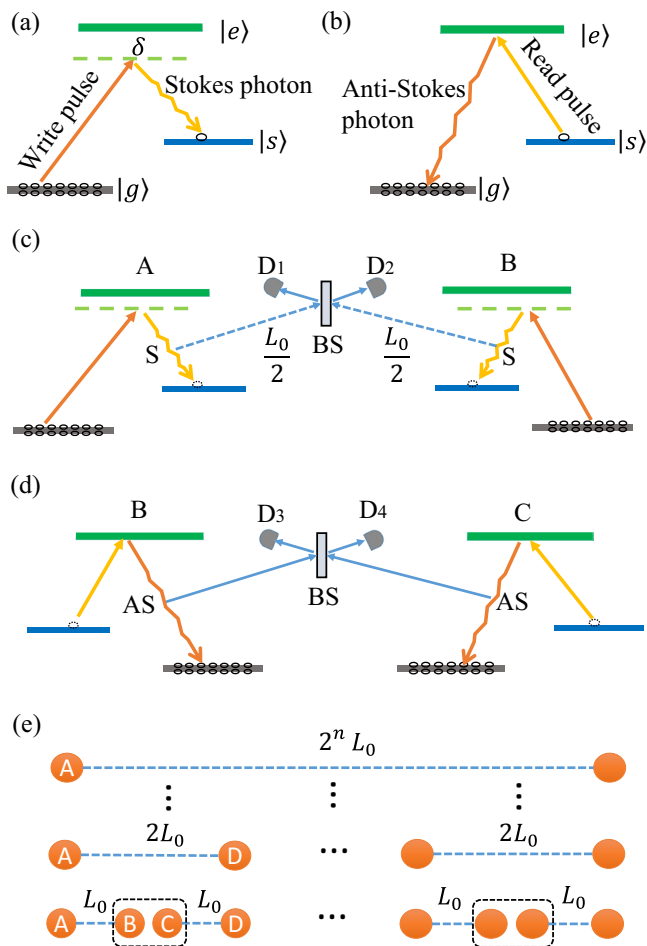
## Results

Various protocols have been proposed for the construction of quantum repeaters based on atomic ensembles<sup>17</sup>. Here, we design our ED proposal based on the Duan–Lukin–Cirac–Zoller (DLCZ) scheme<sup>18</sup>, which is a well-known long-distance quantum communication scheme, proposed by L.-M. Duan, M. D. Lukin, J. I. Cirac & P. Zoller in 2001. It is a typical single-photon hierarchical scheme<sup>17</sup>, which is robust against the low efficiency in transmission<sup>18</sup>. The DLCZ scheme has been successfully demonstrated in diverse physical systems including cold atoms<sup>20,31–35</sup>, hot atoms<sup>36,37</sup>, micro-mechanical oscillators<sup>38,39</sup>, and diamonds<sup>40</sup>. Recently, non-classical correlations were observed in the rare-earth-ion-doped crystal<sup>41–43</sup>, which is a promising solid-state platform for the quantum repeater node due to its unique capability of long-lived optical storage<sup>44,45</sup>.

Here we provide a concise review on the original DLCZ protocol for introducing the following discussions on the entanglement distillation and connection proposal. The DLCZ scheme<sup>18</sup> begins with the entanglement generation (EG) process. Suppose an atomic ensemble possesses two ground states ( $|g\rangle$ ) and an excited state ( $|e\rangle$ ), and all atoms are initialized to the ground state  $|g\rangle$  at the beginning. The ensemble can be excited by a weak and off-resonant laser pulse, inducing Raman transitions to the state  $|s\rangle$ , revealing scattered Stokes photons (Fig. 1a). Considering the relatively small excitation rate  $p_c$ , the state of the atomic ensemble and the Stokes photon can be written as<sup>17,18,46</sup>:

$$|\phi\rangle = |0\rangle_p |0\rangle_a + \sqrt{p_c} |1\rangle_p |1\rangle_a. \quad (1)$$

Here  $|0\rangle_a = \frac{1}{\sqrt{N_A}} \sum_{i=1}^{N_A} |g_i g_2 \cdots g_i \cdots g_{N_A}\rangle_a$ , denotes the ensemble is in the ground state.  $|1\rangle_a = \frac{1}{\sqrt{N_A}} \sum_{i=1}^{N_A} |g_i g_2 \cdots s_i \cdots g_{N_A}\rangle_a$ ,



**Fig. 1 Processes of the Duan-Lukin-Cirac-Zoller scheme.** **a** Write process. An off-resonant laser pulse with detuning of  $\delta$  to  $|g\rangle \rightarrow |e\rangle$  transition induces a Stokes (S) photon with a small probability. **b** Read process. A resonant laser pulse drives single excitation from  $|s\rangle$  to  $|e\rangle$ , inducing an anti-Stokes (AS) photon correlated with the Stokes photon. **c** Entanglement generation process. The Stokes photons revealed by ensemble A and B interfere on a beam splitter (BS). **d** The first level entanglement connection. **e** Extending the communication length by utilizing entanglement connection. The single-photon detector  $D_1$  and  $D_2$  are used to detect the Stokes photon in the entanglement generation process, while  $D_3$  and  $D_4$  are utilized to detect the anti-Stokes photon in the entanglement connection process.  $L_0$  denotes the distance between two neighboring nodes.

denotes the ensemble is charged with a collective excitation.  $|0\rangle_p$  and  $|1\rangle_p$  correspond to the photonic vacuum and single-photon state, respectively. Considering two atomic ensembles (named node A and node B) separated by a distance of  $L_0$ , the Stokes photons emitted by the two ensembles are transmitted and interfere on a beam splitter (BS) at the central station between these two nodes. Successful detection of a single Stokes photon indicates that node A and B are entangled (Fig. 1c), whose state is represented as:

$$|\psi\rangle_{AB} = \frac{1}{\sqrt{2}}(|0\rangle_A|1\rangle_B + e^{i\theta}|1\rangle_A|0\rangle_B), \quad (2)$$

where  $\theta$  denotes the relative phase.

The next step is the EC process. Two pairs of entangled states are established between node A, B and node C, D using the protocol described above. Node A(C) and node B(D) are separated by  $L_0$ , while node B and C are close to each other. The probabilistically stored atomic excitation in node B and C are converted back into anti-Stokes photons by a strong and resonant pulse (Fig. 1b). The induced anti-Stokes photons are combined on a BS between node B and C. Detecting a single anti-Stokes photon suggests the success of the EC process, i.e., node A and D are entangled with each other (Fig. 1d). Their state is written as:

$$|\psi\rangle_{AD} = \frac{1}{\sqrt{2}}(|0\rangle_A|1\rangle_D + e^{i\theta'}|1\rangle_A|0\rangle_D). \quad (3)$$

Therefore, the communication length doubles. Once the EC process has been conducted successfully with  $n$  levels, the total communication length will be extended to  $2^n L_0$  (as shown in Fig. 1e).

**Entanglement distillation proposal.** Taking into account the photon loss in the channel as well as the noise of the single-photon detectors in practice, the state in Eq. (2) is modified into a density matrix:

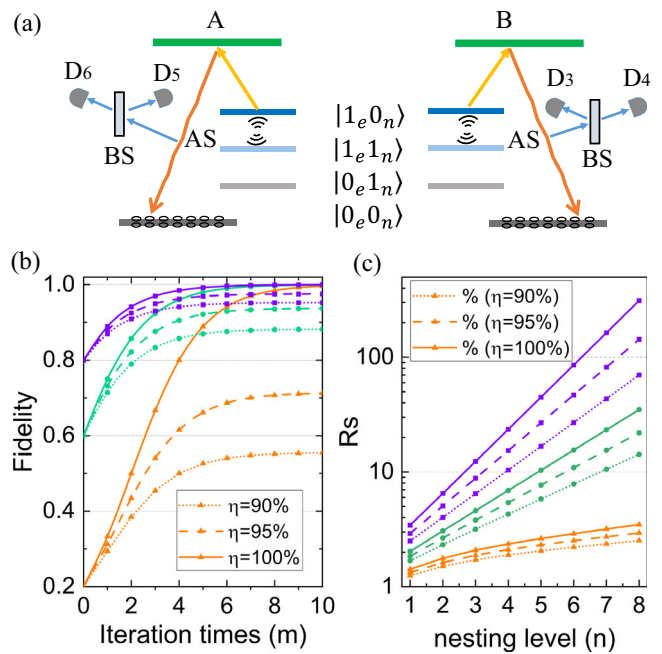
$$\rho_{AB} = \frac{1}{1 + p_2 + p_0} (|\psi\rangle^+ \langle\psi| + p_2|11\rangle_{AB}\langle 11| + p_0|00\rangle_{AB}\langle 00|), \quad (4)$$

where  $|\psi\rangle^+ = \frac{1}{\sqrt{2}}(|01\rangle_{AB} + |10\rangle_{AB})$ , is the target entangled state, hereafter we omit the phase shift for simplicity. Other coherence terms (for instance,  $|11\rangle\langle 10|$  and  $|10\rangle\langle 11|$ ) are neglected<sup>47</sup>, since we are only interested in the coherence property of the target entangled state.  $|11\rangle_{AB}$  represents the multi-photon component which affects the fidelity of the state with the weight of  $p_2$ . It appears due to the event in which both ensembles are excited but only one photon is detected during the EG process.  $|00\rangle_{AB}$  is the vacuum component which reduces the entanglement distribution rate with the weight of  $p_0$ . It comes from the event heralded by the dark count of the single-photon detector. The fidelity can be expressed as:

$$F_0 = \frac{1}{1 + p_2}, \quad (5)$$

where  $F_0 \approx 1 - p_2^{18}$ , with  $p_2 \ll 1$ .

According to Eq. (5), the multi-photon component is the primary source of errors that decrease the fidelity. In the following EC process, this error component dramatically amplifies, thus decreases the fidelity of the distributed entangled state between distant nodes. In the original and the improved DLCZ-like schemes<sup>47,48</sup>, minimizing the excitation probability  $p_c$  to suppress the multi-photon component is a widely-used passive countermeasure to maintain the fidelity of the distributed entangled state<sup>18,47,48</sup>. However, a small  $p_c$  directly



**Fig. 2 The entanglement distillation proposal and its enhancement on entanglement fidelity and rate.** **a** The energy-level diagram and the entanglement distillation proposal. A and B represent two distant communication nodes. The subscript e and n denotes the electron and nuclear degrees of freedom, respectively. Anti-Stokes, AS; beam splitter, BS; Detector, D. **b** The fidelity after entanglement distillation as a function of the iteration times with the initial fidelity of 0.2 (triangle symbol and yellow line), 0.6 (dot symbol and green line) and 0.8 (square symbol and purple line), respectively. **c** The speedup coefficient  $R_s$  as a function of the nesting levels by increasing the excitation rate  $p_c$  and utilizing entanglement distillation after the last level's entanglement connection process.  $p_c = 10^{-3}$  (triangle symbol and yellow line),  $10^{-4}$  (dot symbol and green line),  $10^{-5}$  (square symbol and purple line). The dot, dash, solid line represents the total efficiency  $\eta = 90\%$ ,  $95\%$ ,  $100\%$ , respectively.

translates into a low data rate for entanglement distribution and a long storage time required for the memory. Meanwhile, the dark counts of the single-photon detectors will cause an enormous vacuum component during the EG process when  $p_c$  is smaller than  $10^{-2}$ , hampering the EC process (see explicit calculation in the next section). These inefficiency and demanding requirements have so far limited the implementation of the DLCZ protocol within a short scale. In the following paragraph, we will present an ED proposal to eliminate the multi-photon component in a more practical way.

In atomic ensembles that have coupled electron and nuclear spins (Fig. 2a), state  $|g\rangle$  and  $|s\rangle$  can be represented by  $|0_e0_n\rangle$  and  $|1_e0_n\rangle$ , where the subscript e and n denotes the electron and nuclear degrees of freedom, respectively.  $|\psi\rangle^+$  can be rewritten as:

$$\frac{1}{\sqrt{2}}(|0_e0_n\rangle_A|1_e0_n\rangle_B + |1_e0_n\rangle_A|0_e0_n\rangle_B). \quad (6)$$

$|0_e0_n\rangle_A|1_e0_n\rangle_B = |01\rangle_{AB}$ ,  $|1_e0_n\rangle_A|0_e0_n\rangle_B = |10\rangle_{AB}$ ,  $|1_e0_n\rangle_A|1_e0_n\rangle_B = |11\rangle_{AB}$ ,  $|0_e0_n\rangle_A|0_e0_n\rangle_B = |00\rangle_{AB}$ . As shown in Fig. 2a, a radio frequency (RF)  $\frac{\pi}{2}$  pulse is applied between the spin levels  $|1_e0_n\rangle$  and  $|1_e1_n\rangle$  on ensemble A and B separately. After these operations,  $|0_e0_n\rangle_{A(B)}$  unchanged and  $|1_e0_n\rangle_{A(B)}$  turns to  $\frac{1}{\sqrt{2}}(|1_e0_n\rangle_{A(B)} +$

$|1_e 1_n\rangle_{A(B)}$ ). As a result,

$$\begin{aligned} |0_e 0_n\rangle_A |1_e 0_n\rangle_B &\rightarrow \frac{1}{\sqrt{2}} (|0_e 0_n\rangle_A |1_e 0_n\rangle_B + |0_e 0_n\rangle_A |1_e 1_n\rangle_B), \\ |1_e 0_n\rangle_A |0_e 0_n\rangle_B &\rightarrow \frac{1}{\sqrt{2}} (|1_e 0_n\rangle_A |0_e 0_n\rangle_B + |1_e 1_n\rangle_A |0_e 0_n\rangle_B), \\ |1_e 0_n\rangle_A |1_e 0_n\rangle_B &\rightarrow \frac{1}{2} (|1_e 0_n\rangle_A |1_e 0_n\rangle_B + |1_e 0_n\rangle_A |1_e 1_n\rangle_B \\ &\quad + |1_e 1_n\rangle_A |1_e 0_n\rangle_B + |1_e 1_n\rangle_A |1_e 1_n\rangle_B). \end{aligned}$$

Then the excitations on  $|1_e 0_n\rangle$  are retrieved and the induced anti-Stokes photons are detected. Only when  $D_3, D_4, D_5,$  and  $D_6$  (as shown in Fig. 2a, these detectors are already assembled in the EC processes) both record no click, the distillation process is successful. Otherwise, the ensembles are initialized and the previous steps are repeated. The successful probability is  $\frac{1}{2}$  for the  $|\psi\rangle^+$  component,  $\frac{1}{4}$  for the  $|11\rangle_{AB}$  and 1 for the  $|00\rangle_{AB}$  component, assuming perfect retrieval and detection efficiency. Upon success, a  $\pi$  pulse is applied between  $|1_e 0_n\rangle$  and  $|1_e 1_n\rangle$  on ensemble A and B separately, to bring back the useful  $|\psi\rangle^+$  state. The remained state after distillation is:

$$\frac{1}{1 + p_2/2 + 2p_0} (|\psi\rangle^+ \langle\psi| + \frac{p_2}{2} |11\rangle_{AB} \langle 11| + 2p_0 |00\rangle_{AB} \langle 00|). \quad (7)$$

The fidelity increases to  $F_1 = \frac{1}{1+p_2/2}$ . The distillation process can be conducted for many times. After  $n$  levels' distillation, the fidelity is improved to  $F_n = \frac{1}{1+p_2/2^n}$ . The fidelity of the entangled state after the ED process monotonously increases as the iteration time grows, even if taking the imperfections of the memories and detectors into account (as shown in Fig. 2b), the detailed analysis and calculations are provided in Supplementary Note 1 and Supplementary Fig. 1. To effectively implement our protocol, a high detection and memory efficiency (>50%) are required, which can be achieved by utilizing impedance-match optical cavity to enhance the memory efficiency<sup>49</sup> and efficient detectors to maximize the detection efficiency<sup>50</sup>.

The proposal has no restriction on the fidelity of the raw state, thus the distillation process can be applied at any level of the EG and ES steps, which is not allowed for the previous entanglement purification schemes<sup>8,9,23</sup>.

**Accelerating entanglement distribution with entanglement distillation.** Now we will show that the ED introduced above can help accelerate the entanglement distribution rate, considering the dark counts of single-photon detectors in realistic situations. Suppose an entangled state is established between node A and B during the EG process. The excitation rate is  $p_c$ , then the state is written as:

$$\rho = \frac{1}{1 + p_c + p_0} (|\psi\rangle \langle\psi| + p_c |11\rangle \langle 11| + p_0 |00\rangle \langle 00|). \quad (8)$$

$p_0$  is the vacuum coefficient, and is expressed as<sup>18</sup>

$$p_0 = \frac{p_{dc}}{p_c \eta_p}, \quad (9)$$

$$\eta_p = \eta_t \eta_o \eta_d. \quad (10)$$

Here,  $p_{dc}$  is the probability of recording a click caused by dark count of the detector in a single detection window,  $\eta_t = 10^{-\frac{L_0}{2L_{att}}}$  is the channel attenuation,  $L_0$  is the distance between two neighboring repeater stations,  $L_{att} = 40$  km is the attenuation length of the channel.  $\eta_o$  results from other noise (for instance,

the spontaneous emissions in the atomic ensembles and the coupling inefficiency of the photons into and out of the channel), and is independent of the communication distance.  $\eta_d$  is the detection efficiency.  $\eta_p$  is the overall efficiency. For a typical elementary link distance  $L_0 = 160$  km,  $\eta_t = 10^{-2}$ . Suppose the realistic single-photon detectors have a dark count rate of 10 Hz and a detection window of 100 ns,  $p_{dc} = 10^{-6}$ . The fidelity is written as

$$F = \frac{1}{1 + p_c}. \quad (11)$$

The entanglement generation rate is defined as:

$$R_g = p_c \eta_p. \quad (12)$$

Considering the memory efficiency of  $\eta_m$ , let

$$\eta = \eta_m \eta_d, \quad (13)$$

the entangled state after the  $i$ -th level EC process can be expressed as

$$\rho_{(i)} = \frac{1}{1 + p_{2(i)} + p_{0(i)}} (|\psi\rangle^+ \langle\psi| + p_{2(i)} |11\rangle \langle 11| + p_{0(i)} |00\rangle \langle 00|), \quad (14)$$

where,  $p_{0(0)} = p_0, p_{2(0)} = p_c, p_{2(i)} = 2p_{2(i-1)}$ , for  $i \geq 1$ . For the conventional single-photon detectors that do not have photon number resolution,  $p_{0(i)} = 2p_{0(i-1)} + \frac{1}{2}(2 - \eta)$ . The successful establishment of the entangled state between two distant nodes requires the success of the EC processes at all levels, whose probability is expressed as:

$$P_{tot} = \left(\frac{2}{3}\right)^n P_{s(1)} P_{s(2)} \dots P_{s(i)} \dots P_{s(n)}, \quad (15)$$

where

$$\begin{aligned} P_{s(i)} &= \frac{\frac{1}{2} + \frac{(2-\eta)}{4} + p_{2(i-1)} + p_{0(i-1)}}{(1 + p_{0(i-1)} + p_{2(i-1)})^2} \eta \\ &\approx \frac{1 - \frac{\eta}{4} + p_{0(i-1)}}{(1 + p_{0(i-1)})^2} \eta \end{aligned} \quad (16)$$

is the successful probability of the  $i$ -th level's EC process. The coefficient  $\frac{2}{3}$  is due to the fact that for every  $i$ -th level EC process one has to establish two nearby links at the  $(i-1)$ -th level in advance, considering the low transmissivity regime<sup>17</sup>. The total entanglement distribution rate is

$$R_{tot} = R_g P_{tot}. \quad (17)$$

A large vacuum component will be generated and the entanglement distribution rate will be slowed down when  $p_c$  is quite small. In order to suppress the effect of massive vacuum component, we can increase the excitation rate  $p_c$  to  $p'_c$  in the EG process, and utilizing the ED process after the last level's EC process to achieve the identical fidelity. The state with excitation rate of  $p'_c$  is

$$\rho' = \frac{1}{1 + p'_c + p'_0} (|\psi\rangle^+ \langle\psi| + p'_c |11\rangle \langle 11| + p'_0 |00\rangle \langle 00|),$$

$$p'_0 = \frac{p_{dc}}{p'_c \eta_p}.$$

$$F' = \frac{1}{1 + p'_c}.$$

$$R'_g = p'_c \eta_p. \quad (18)$$

The total entanglement distribution rate with excitation rate of  $p'_c$



and nesting level of  $n$  is

$$R'_{tot} = R'_g P'_{tot} P'_d. \quad (19)$$

Where,  $P'_{tot}$  is the probability that all the EC processes are successful with the excitation rate  $p'_c$ ,  $P'_d$  is the successful probability of the ED process.

Here we define a parameter

$$R_s = \frac{R'_{tot}}{R_{tot}} \quad (20)$$

to quantitatively characterize the speedup effect of our proposal. Figure 2c shows the speedup effect for different nesting levels (see explicit calculation in Supplementary Note 2).

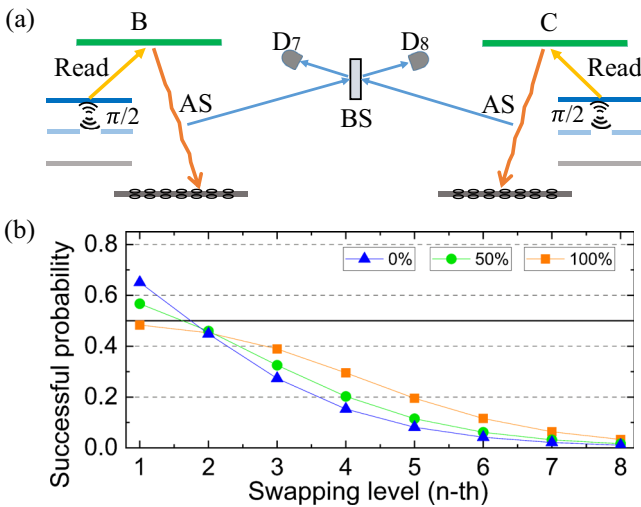
**Improvement of the entanglement connection process.** The LOs and detection also can be utilized to improve the EC process. Suppose two pairs of entangled state have been generated between node A, B and node C, D. The state  $|\Psi\rangle_{ABCD}$  is:

$$\frac{1}{2}(|0_A 1_B 0_C 1_D\rangle + |1_A 0_B 1_C 0_D\rangle + |0_A 1_B 1_C 0_D\rangle + |1_A 0_B 0_C 1_D\rangle).$$

EC process is based on detection of the interference of the anti-Stokes photons emitted by B and C, and is successful when only one click is recorded by the detectors. However, the  $|0_A 1_B 1_C 0_D\rangle$  component also causes only one click if the detectors have no full photon number resolution, inducing a vacuum component  $|0_A 0_D\rangle$ <sup>17,47</sup>. The state after the EC process can be written as

$$\rho_{AD} = \frac{1}{1 + p_{0(1)}} (|\psi\rangle_{AD}\langle\psi| + p_{0(1)}|00\rangle_{AD}\langle 00|), \quad (21)$$

where  $|\psi\rangle_{AD}$  is similar as  $|\psi\rangle_{AB}$ ,  $p_{0(1)}$  is the coefficient of the vacuum component generated during the EC process. This component amplifies during the later EC processes, decreases the successful probabilities of the EC processes and reduces the entanglement distribution rate. Figure 3b illustrates the successful probabilities of the EC processes as a function of the swapping levels, utilizing the single-photon detector with different photon



**Fig. 3 Improving the entanglement connection process.** **a** Scheme for optimization of the entanglement connection process. B and C are two adjacent nodes. Anti-Stokes, AS; beam splitter, BS; Detector, D. **b** The successful probabilities of the entanglement connection process as a function of the swapping levels ( $n$ ) utilizing single-photon detectors with photon number resolution of 0 (triangle), 50% (dot), and 100% (square). Here we have assumed the total efficiency  $\eta = 0.9$  and excitation rate  $p_c = 0.001$ .

number resolution.  $p_{0(1)} = 1 - \frac{1}{2}\eta$  for the conventional single-photon detectors that do not possess photon number resolution.

We propose that the LOs and detection can mimic the function of the photon-number resolving detector, which is currently a technology in development<sup>51,52</sup>. The EC processes can be optimized as follows (Fig. 3a).

As displayed in Fig. 2a,  $|0_A 1_B 1_C 0_D\rangle$  can be rewritten as  $|0_e 0_n\rangle_A |1_e 0_n\rangle_B |1_e 0_n\rangle_C |0_e 0_n\rangle_D$ , in the same way,  $|0_A 1_B 0_C 1_D\rangle = |0_e 0_n\rangle_A |1_e 0_n\rangle_B |0_e 0_n\rangle_C |1_e 0_n\rangle_D$ ,  $|1_A 0_B 1_C 0_D\rangle = |1_e 0_n\rangle_A |0_e 0_n\rangle_B |1_e 0_n\rangle_C |0_e 0_n\rangle_D$ ,  $|1_A 0_B 0_C 1_D\rangle = |1_e 0_n\rangle_A |0_e 0_n\rangle_B |0_e 0_n\rangle_C |1_e 0_n\rangle_D$ . First, a  $\frac{\pi}{2}$  pulse is applied between  $|1_e 0_n\rangle$  and  $|1_e 1_n\rangle$  on ensemble B and C separately. In this case,

$$\begin{aligned} |1_e 0_n\rangle_B |0_e 0_n\rangle_C &\rightarrow \frac{1}{\sqrt{2}}(|1_e 0_n\rangle_B |0_e 0_n\rangle_C + |1_e 1_n\rangle_B |0_e 0_n\rangle_C) \\ |0_e 0_n\rangle_B |1_e 0_n\rangle_C &\rightarrow \frac{1}{\sqrt{2}}(|0_e 0_n\rangle_B |1_e 0_n\rangle_C + |0_e 0_n\rangle_B |1_e 1_n\rangle_C) \\ |1_e 0_n\rangle_B |1_e 0_n\rangle_C &\rightarrow \frac{1}{2}(|1_e 0_n\rangle_B |1_e 0_n\rangle_C + |1_e 0_n\rangle_B |1_e 1_n\rangle_C \\ &\quad + |1_e 1_n\rangle_B |1_e 0_n\rangle_C + |1_e 1_n\rangle_B |1_e 1_n\rangle_C). \end{aligned}$$

Then, the excitation on  $|1_e 0_n\rangle$  of ensemble B and C is retrieved simultaneously.

Second, a  $\pi$  pulse between  $|1_e 0_n\rangle$  and  $|1_e 1_n\rangle$  is applied, following another retrieving process on  $|1_e 0_n\rangle$ . The success of the EC process is defined as the case when only one click is recorded during the two retrieving processes. As a result, the coefficient of the vacuum component  $p_{0(1)}$  is modified to  $1 - \frac{3}{4}\eta$  (see explicit calculation in Supplementary Note 3).

Moreover, the single retrieving process can be divided to  $2^l$  ( $l \geq 1$ ) times, once we have  $2^l$  sub-levels. Then the coefficient of the vacuum component can be further written to

$$p_{0(1)} = 1 - \eta + \frac{1}{4^l} \eta, \quad (22)$$

a specific example and detailed considerations has been provided in Supplementary Note 3.

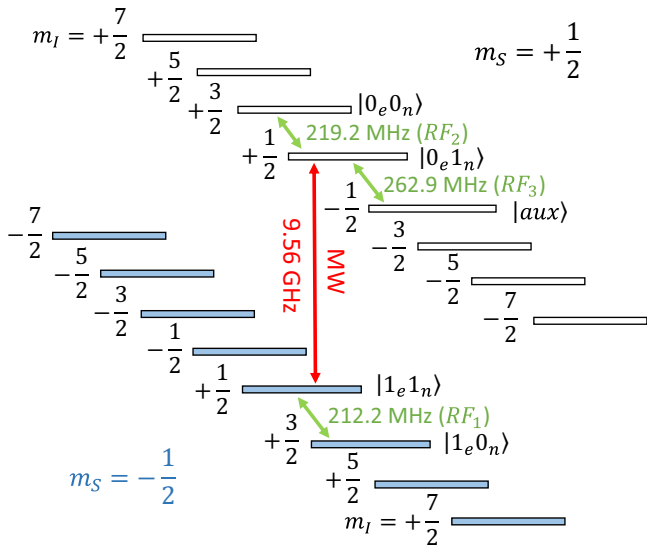
The  $|0_A 1_B 1_C 0_D\rangle$  component can be almost fully distinguished with a high  $l$ , which is equal to the function of the fully-photon-number-resolving detector. Such high dimensional Hilbert space can be obtained in rare-earth material with nuclear spin of high quantum numbers<sup>53,54</sup>. Hence, the  $|0_A 0_D\rangle$  component is minimized after the EC process.

**Initial experiments.** These LOs on the hybrid spin levels are the primary requirements for our ED proposal for the atomic-ensemble-based quantum node. The functions of the  $\frac{\pi}{2}$  and  $\pi$  pulses employed here are similar to the transformations result from the controlled Hadamard and CNOT gates between electron and nuclear spins<sup>55,56</sup>, whose fidelity determines the final entanglement fidelity as well as the entanglement distribution rate. Here we demonstrate these operations with high fidelity in an actual physical system, i.e., a  $^{143}\text{Nd}^{3+}:\text{Y}_2\text{SiO}_5$  crystal. This material is chosen because of its large Hilbert space, with electron spin  $S = \frac{1}{2}$  and nuclear spin  $I = \frac{7}{2}$ <sup>30,54</sup>. By combining series of these LOs and an efficient initial state preparation, we can prepare a high-fidelity entangled state between the electron and nuclear spins.

The spin Hamiltonian of our system is represented as<sup>30,54</sup>:

$$H = \mu_B \mathbf{B}_0 \cdot \mathbf{g} \cdot \mathbf{S} + \mathbf{S} \cdot \mathbf{A} \cdot \mathbf{I}. \quad (23)$$

Here  $\mu_B$  is the Bohr magneton,  $\mathbf{A}$  and  $\mathbf{g}$  are the hyperfine and  $g$  tensors, respectively, and  $\mathbf{I}$  ( $\mathbf{S}$ ) denotes the nuclear (electron) spin operator. The corresponding energy-level diagram is shown in Fig. 4. Here we have chosen  $|\pm \frac{1}{2}\rangle_e |\pm \frac{1}{2}\rangle_n$ ,  $|\pm \frac{1}{2}\rangle_e |\pm \frac{3}{2}\rangle_n$ , and



**Fig. 4** The energy-level structure of the  $4I_{9/2}(0)$  state of  $^{143}\text{Nd}^{3+}:\text{Y}_2\text{SiO}_5$  under an external magnetic field of  $B_0 = 439.8 \text{ mT}$ . The red arrow indicates the electron-spin-resonance transition between the  $|+\frac{1}{2}\rangle_e |+\frac{1}{2}\rangle_n$  and  $|-\frac{1}{2}\rangle_e |+\frac{1}{2}\rangle_n$  state. The green arrows represent the relevant nuclear-magnetic-resonance transitions, whose frequencies are also labeled.  $|aux\rangle$  represent the auxiliary energy level.  $m_s$  and  $m_l$  denote the electron and nuclear spin quantum number, respectively. Microwave, MW; radio-frequency, RF.

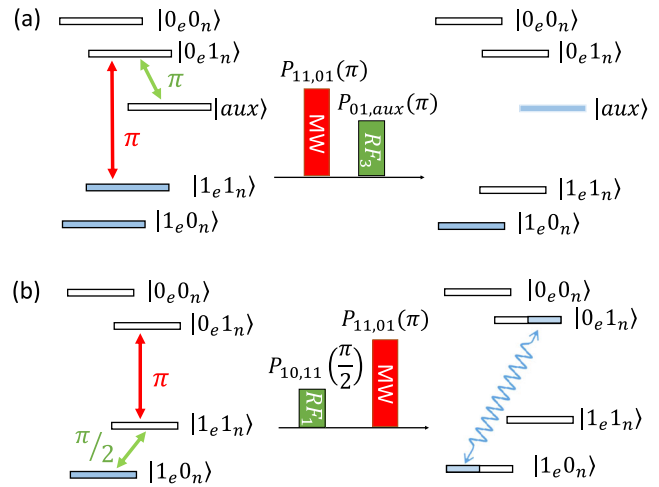
$|+\frac{1}{2}\rangle_e |-\frac{1}{2}\rangle_n$  to conduct the experiments. We encode  $|-\frac{1}{2}\rangle_e (|+\frac{1}{2}\rangle_e)$  as  $|1\rangle_e (|0\rangle_e)$  and  $|+\frac{1}{2}\rangle_n (|+\frac{3}{2}\rangle_n)$  as  $|1\rangle_n (|0\rangle_n)$  for simplicity. The four orthogonal states can be rewritten as  $|0_e 0_n\rangle, |0_e 1_n\rangle, |1_e 0_n\rangle, |1_e 1_n\rangle$ , forming a two-qubit subspace.  $|+\frac{1}{2}\rangle_e |-\frac{1}{2}\rangle_n$  is labeled as  $|aux\rangle$ , and is employed to transfer the unwanted population. The associated electron-spin-resonance (ESR) transition ( $\Delta m_s = \pm 1, \Delta m_l = 0$ ) and nuclear-magnetic-resonance (NMR) transitions ( $\Delta m_s = 0, \Delta m_l = \pm 1$ ) are labeled as MW (9.56 GHz),  $RF_1$  (212.2 MHz),  $RF_2$  (219.2 MHz), and  $RF_3$  (262.9 MHz), respectively. The NMR transition frequencies are measured and identified at 100 mK utilizing the method introduced by Pei-Yun et al.<sup>54</sup>. In the two-qubit subspace, the Bell state is written as:

$$|\Psi\rangle^\pm = \frac{1}{\sqrt{2}} (|0_e 1_n\rangle \pm |1_e 0_n\rangle), \quad (24)$$

$$|\Phi\rangle^\pm = \frac{1}{\sqrt{2}} (|0_e 0_n\rangle \pm |1_e 1_n\rangle). \quad (25)$$

Here we prepare the  $|\Psi\rangle^+$  state by combining series of these spin operations and an efficient initial state preparation. Our experiment proceeds in two steps: (1) initialization and entanglement generation, (2) tomography of the density matrices.

For a thermal equilibrium state, the populations are predominantly determined by the electron spin polarization, which is expressed as  $\alpha = e^{-\frac{g\mu_B B_0}{k_B T}}$ <sup>57</sup>, where  $B_0$  is the magnetic field,  $g$  is the electron g-factor, and  $T$  is the sample temperature. In a previous work, a high field (3.4 T) and a low temperature (2.9 K) are combined to polarize the electron spins of phosphorus doped in silicon to 66%<sup>57</sup>. Here, the electron spins approach fully polarized ( $\alpha = 1.02\%$ ) with a modest magnetic field of 439.8 mT with the assistance of an ultra-low sample temperature of 100 mK<sup>54</sup>. As



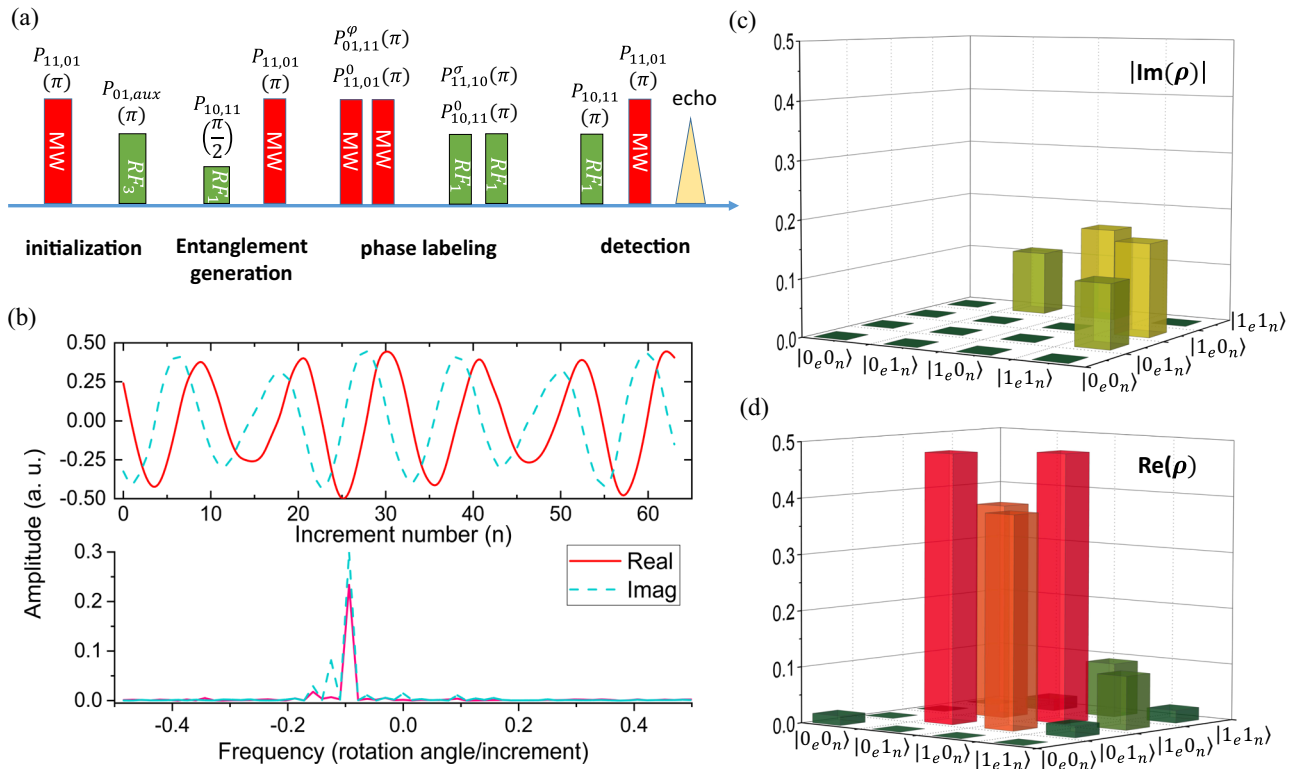
**Fig. 5** Sequences for initialization and entanglement generation process. **a** Preparation of the initial state. A microwave (MW)  $\pi$  pulse and radio-frequency (RF)  $\pi$  pulse are applied successively to achieve the population inversion between  $|1_e 1_n\rangle$  and the auxiliary energy level  $|aux\rangle$ . Hence, an almost pure initial state is presented in the two-qubit subspace. **b** Generation of the entangled state between the electron and nuclear spins. A RF  $\pi/2$  generates the superposition between  $|1_e 0_n\rangle$  and  $|1_e 1_n\rangle$ , then a MW  $\pi$  pulse is applied between  $|1_e 1_n\rangle$  and  $|0_e 1_n\rangle$ , inducing the entangled state:  $\frac{1}{\sqrt{2}} (|0_e 1_n\rangle + |1_e 0_n\rangle)$ . P denotes pulse.

shown in Fig. 5a, starting from the thermal equilibrium state, a MW pulse  $P_{11,01}(\pi)$  and a RF pulse  $P_{01,aux}(\pi)$  are applied successively to create an almost pure initial state  $|1_e 0_n\rangle$  in the 4-dimensional subspace. Then,  $|\Psi\rangle^+$  can be generated by applying  $P_{10,11}(\frac{\pi}{2})$  and  $P_{11,01}(\pi)$  on the initial state one after another, as shown in Fig. 5b. The other entangled states can be achieved by using different pulse sequences. For instance, applying  $P_{10,11}(\pi), P_{11,01}(\frac{\pi}{2}), P_{01,00}(\pi)$  on the initial state successively will produce  $|\Phi\rangle^+$ .

In order to characterize the fidelity of the spin operations and the degree of the entanglement, we employ density matrix tomography to reveal the initial state and the final entangled state<sup>55,57–61</sup>. For the initial state, we only need to determine the diagonal elements since no coherence is excited during the initialization process. By mapping different pairs of population difference into the electron spin echo between the  $|1_e 1_n\rangle$  and  $|0_e 1_n\rangle$  state, and comparing the echo amplitude with that of the thermal equilibrium state, the corresponding diagonal elements can be obtained. The experimental result is:

$$\rho_i^{exp} = \begin{pmatrix} 0.011 & 0 & 0 & 0 \\ 0 & 0.051 & 0 & 0 \\ 0 & 0 & 0.933 & 0 \\ 0 & 0 & 0 & 0 & 0.005 \end{pmatrix}. \quad (26)$$

Here we use the formula  $F_{\text{state}} = \text{tr} \sqrt{\sqrt{\rho^{th}} \rho^{exp} \sqrt{\rho^{th}}}$ <sup>57,62,63</sup> to calculate the state fidelity,  $\rho^{th}$  and  $\rho^{exp}$  denote the theoretical and experimental density matrix, respectively. The fidelity compared with the target initial state  $\rho_i^{th} = \text{diag}\{\frac{\alpha}{1+3\alpha}, \frac{\alpha}{1+3\alpha}, \frac{1}{1+3\alpha}, \frac{\alpha}{1+3\alpha}\}$  is 99.1(4)%, indicating the reliability of the initial state preparation process. Starting from this initial state, two selective pulses  $P_{10,11}(\frac{\pi}{2})$  and  $P_{11,01}(\pi)$  will produce the target entangled state in theory (with the absence of pulse imperfections and



**Fig. 6 Reconstruction of the density matrix.** **a** The complete pulse sequences for initialization, entanglement generation, geometric phase labeling, and detection for extracting the  $|1_e0_n\rangle\langle 0_e1_n|$  element. Microwave, MW; radio-frequency, RF. P denotes pulse. **b** The oscillation of the echo amplitude acquired by quadrature detection and the corresponding Fourier transform spectrum. The solid lines and dash lines represent the real (in-phase) and imaginary (quadrature) component, respectively. Imag denotes the imaginary part. **c, d** The reconstructed density matrix shown in the basis of hybrid-spin system. The zero elements are displayed with green shading.

decoherence):

$$\rho_f^{th} = \begin{pmatrix} 0.011 & 0 & 0 & 0 \\ 0 & 0.469 & 0.464 & 0 \\ 0 & 0.464 & 0.469 & 0 \\ 0 & 0 & 0 & 0.051 \end{pmatrix}. \quad (27)$$

Now we turn to the reconstruction of the final entangled state. The determination of the diagonal elements of the final entangled state is the same as that of the initial state. The detection of the off-diagonal elements is more complicated. Here we follow the method introduced by Stephanie et al.<sup>57</sup> to add different geometric phases for each pair of the states before detecting their coherence. A pair of pulses  $P_{ij}^\varphi(\pm\pi)$  (or  $P_{ij}^\sigma(\pm\pi)$ ) are applied along different axes on the Bloch sphere spanned by a pair of states  $|i\rangle$  and  $|j\rangle$ , where the superscript denotes the nominal rotation axes with angle  $\varphi$  (or  $\sigma$ ). Each state accumulates a geometric phase which is equal to half of the solid angle of its trajectory on the Bloch sphere<sup>57,64,65</sup>. The effect of the two pulses can be described as an operation  $e^{-i\varphi}|i\rangle\langle i| + e^{i\varphi}|j\rangle\langle j|$  (or  $e^{-i\sigma}|i\rangle\langle i| + e^{i\sigma}|j\rangle\langle j|$ ) with a geometric phase  $\varphi$  (or  $\sigma$ ).

As the experiments repeated,  $\varphi$  and  $\sigma$  increase with different steps. Thus, the difference of the geometric phases between different pair of states is modulated with a particular frequency. Hence, the echo amplitudes are also modulated when mapping the coherence between different pair of states into population difference between  $|1_e1_n\rangle$  and  $|0_e1_n\rangle$ . The modulation frequency varies for different pairs of states. Thus the off-diagonal element

of the density matrix (i.e., the coherence between a pair of states  $|i\rangle$  and  $|j\rangle$ ) can be identified at a particular frequency corresponding to the labeled geometric phase of the Fourier component. As a specific example, Fig. 6a illustrates the complete pulse sequence for initialization, entanglement generation, phase labeling, and detection of the  $|1_e0_n\rangle\langle 0_e1_n|$  element. Figure 6b shows the corresponding oscillation of the echo amplitude utilizing quadrature detection. Other off-diagonal elements relevant to  $|0_e0_n\rangle$  are zero due to the fact that the excitation bandwidths of the MW and RF pulses are relatively small and no coherence could have been generated there<sup>55</sup>. At last, we obtain the full density matrix of the final entangled state:

$$\rho_f^{exp} = \begin{pmatrix} 0.017 & 0 & 0 & 0 \\ 0 & 0.481 & 0.380 & 0.021 + 0.110i \\ 0 & 0.380 & 0.480 & 0.095 + 0.161i \\ 0 & 0.021 - 0.110i & 0.095 - 0.161i & 0.022 \end{pmatrix}. \quad (28)$$

Here we have applied a global phase correction to cancel the imaginary part of the  $|1_e0_n\rangle\langle 0_e1_n|$  element<sup>61</sup>. Figure 6c and d displays the real and imaginary part of the density matrix.

The fidelity of the generated entangled state with respect to the target entangled state is calculated as 94.1(8)%. The fidelity compared with the Bell state is determined as 92.7(8)%, and the corresponding concurrence is calculated as  $C = 0.75$ , which is greatly enhanced compared with the previous work<sup>57</sup>, indicating the high quality of the generated entangled state. The reduction of the state fidelity from 99.1(4)% to 94.1(8)% is mainly due to the

loss of the coherence during the phase labeling and detection process and the pulse imperfections. The operation fidelity is determined as  $F_g = 97.2\%$  (see Supplementary Note 4 for details). The infidelity is due to the inhomogeneous broadening of electron spins, and can be eliminated by applying composite pulses<sup>66–68</sup>. We point out that, the fidelity and concurrence of the final entangled state will be upgraded when taking the decoherence effect into account. As a result, the operation fidelity of  $F_g = 97.2\%$  is actually a lower bound.

**Conclusion.** We propose a specific positive-operator valued measure of the filtering protocol which can be effectively implemented on the ensemble-based quantum nodes. This proposal only requires the LOs applied on the hybrid electron-nuclear spins along with the detection of single photons, and has no restriction on the fidelity of the raw state. By demonstrating these LOs with fidelity as high as 97.2%, a high-quality entangled state is established between the electron and nuclear spins in a rare-earth-ion-doped crystal. Combined with the DLCZ or the DLCZ-like quantum repeater schemes<sup>17,47,48</sup>, our proposal can upgrade the fidelity of the distributed entangled state as well as increase the entanglement distribution rate. Our proposal can also be adapted to other quantum repeater schemes, for instance, achieving partial readout of the anti-Stokes photon by applying high-fidelity spin operations<sup>17</sup>.

Improvements in the near future can be expected by several approaches: First, in our ED proposal, only the errors from multi-photon excitation and vacuum state is considered. However, the current distillation proposal is fully compatible with the specially designed protocol to further correct the phase errors as shown by Jiang et al.<sup>47</sup> and Nicolas et al.<sup>69</sup>. Second, the LO itself is a powerful method to counteract unavoidable decoherence and imperfections during the whole process. Using optimal pulse parameters design and advanced composite pulse sequences<sup>66–68</sup> can increase the fidelity to reach the fault-tolerance threshold. Finally, the method developed provides the toolkit to explore similar platforms such as other solid-state spin systems.

## Methods

The sample is a  $^{143}\text{Nd}^{3+}:\text{Y}_2\text{SiO}_5$  crystal. It has a dopant concentration of 20 ppm and the  $^{143}\text{Nd}$  has an isotope enrichment of 91%. The crystal is cut along its optical axes, i.e.,  $D_1$ ,  $D_2$ , and  $b^{70}$ , with dimensions of  $1.2 \times 1.0 \times 1.4$  mm. With the help of a home-built sub-Kelvin pulsed electron-nuclear-double-resonance (ENDOR) spectrometer, the sample can be faithfully cooled to 100 mK (see detail in the work of Pei-Yun<sup>54</sup>).

The spectrometer can generate Microwave (MW) and radio-frequency (RF) pulses with peak power of 20 and 100 W, which can be utilized to coherently drive the electron and nuclear spins. An electromagnet provides a magnetic field of 439.8 mT along the  $D_1$  axis of the crystal, inducing a Zeeman splitting of the electron spin levels of 9.56 GHz, matching the resonant frequency of the resonator. Typically, the duration of the MW (RF)  $\pi$  pulse is 50 ns (1  $\mu\text{s}$ ) in our experiments.

## Data availability

The data that support the findings of this study are available from the corresponding author upon reasonable request.

## Code availability

All codes used to produce the findings of this study are available from the corresponding author upon reasonable request.

Received: 30 July 2021; Accepted: 17 February 2022;

Published online: 22 March 2022

## References

1. Bennett, C. H. & Brassard, G. Quantum cryptography: public key distribution and coin tossing. in *Proceedings of the International Conference on Computers, Systems and Signal Processing* (1984).

2. Ekert, A. K. Quantum cryptography based on Bell theorem. *Phys. Rev. Lett.* **67**, 661–663 (1991).
3. Bennett, C. H. et al. Teleporting an unknown quantum state via dual classical and Einstein-Podolsky-Rosen channels. *Phys. Rev. Lett.* **70**, 1895–1899 (1993).
4. Cirac, J. I., Ekert, A. K., Huelga, S. F. & Macchiavello, C. Distributed quantum computation over noisy channels. *Phys. Rev. A* **59**, 4249–4254 (1999).
5. Gottesman, D., Jennewein, T. & Croke, S. Longer-baseline telescopes using quantum repeaters. *Phys. Rev. Lett.* **109**, 070503 (2012).
6. Komar, P. et al. A quantum network of clocks. *Nat. Phys.* **10**, 582–587 (2014).
7. Giovannetti, V., Lloyd, S. & Maccone, L. Advances in quantum metrology. *Nat. Photonics* **5**, 222–229 (2011).
8. Deutsch, D. et al. Quantum privacy amplification and the security of quantum cryptography over noisy channels. *Phys. Rev. Lett.* **77**, 2818–2821 (1996).
9. Bennett, C. H. et al. Purification of noisy entanglement and faithful teleportation via noisy channels. *Phys. Rev. Lett.* **76**, 722–725 (1996).
10. Duan, L. M., Giedke, G., Cirac, J. I. & Zoller, P. Entanglement purification of Gaussian continuous variable quantum states. *Phys. Rev. Lett.* **84**, 4002–4005 (2000).
11. Pan, J.-W., Simon, C., Brukner, Č. & Zeilinger, A. Entanglement purification for quantum communication. *Nature* **410**, 1067–1070 (2001).
12. Kwiat, P. G., Barraza-Lopez, S., Stefanov, A. & Gisin, N. Experimental entanglement distillation and ‘hidden’ non-locality. *Nature* **409**, 1014–1017 (2001).
13. Pan, J. W., Gasparoni, S., Ursin, R., Weihs, G. & Zeilinger, A. Experimental entanglement purification of arbitrary unknown states. *Nature* **423**, 417–422 (2003).
14. Walther, P. et al. Quantum nonlocality obtained from local states by entanglement purification. *Phys. Rev. Lett.* **94**, 040504 (2005).
15. Kalb, N. et al. Entanglement distillation between solid-state quantum network nodes. *Science* **356**, 928–932 (2017).
16. Reichle, R. et al. Experimental purification of two-atom entanglement. *Nature* **443**, 838–841 (2006).
17. Sangouard, N., Simon, C., de Riedmatten, H. & Gisin, N. Quantum repeaters based on atomic ensembles and linear optics. *Rev. Mod. Phys.* **83**, 33–80 (2011).
18. Duan, L. M., Lukin, M. D., Cirac, J. I. & Zoller, P. Long-distance quantum communication with atomic ensembles and linear optics. *Nature* **414**, 413–8 (2001).
19. Chou, C. W. et al. Functional quantum nodes for entanglement distribution over scalable quantum networks. *Science* **316**, 1316–1320 (2007).
20. Yu, Y. et al. Entanglement of two quantum memories via fibres over dozens of kilometres. *Nature* **578**, 240–+ (2020).
21. Liu, X. et al. Heralded entanglement distribution between two absorptive quantum memories. *Nature* **594**, 41–45 (2021).
22. Lago-Rivera, D., Grandi, S., Rakonjac, J. V., Seri, A. & de Riedmatten, H. Telecom-heralded entanglement between multimode solid-state quantum memories. *Nature* **594**, 37–40 (2021).
23. Briegel, H. J., Dür, W., Cirac, J. I. & Zoller, P. Quantum repeaters: the role of imperfect local operations in quantum communication. *Phys. Rev. Lett.* **81**, 5932–5935 (1998).
24. Dür, W., Briegel, H. J., Cirac, J. I. & Zoller, P. Quantum repeaters based on entanglement purification. *Phys. Rev. A* **59**, 169–181 (1999).
25. Verstraete, F., Dehaene, J. & DeMoor, B. Local filtering operations on two qubits. *Phys. Rev. A* **64**, 010101 (2001).
26. Dür, W. & Briegel, H. J. Entanglement purification and quantum error correction. *Rep. Prog. Phys.* **70**, 1381–1424 (2007).
27. Usmani, I., Afzelius, M., Riedmatten, H. D. & Gisin, N. Mapping multiple photonic qubits into and out of one solid-state atomic ensemble. *Nat. Commun.* **1**, 12 (2010).
28. Clausen, C. et al. Quantum storage of photonic entanglement in a crystal. *Nature* **469**, 508–U579 (2011).
29. Usmani, I. et al. Heralded quantum entanglement between two crystals. *Nat. Photonics* **6**, 234–237 (2012).
30. Wolfowicz, G. et al. Coherent storage of microwave excitations in rare-earth nuclear spins. *Phys. Rev. Lett.* **114**, 170503 (2015).
31. Kuzmich, A. et al. Generation of nonclassical photon pairs for scalable quantum communication with atomic ensembles. *Nature* **423**, 731–734 (2003).
32. Matsukevich, D. N. & Kuzmich, A. Quantum state transfer between matter and light. *Science* **306**, 663–666 (2004).
33. Chou, C. W. et al. Measurement-induced entanglement for excitation stored in remote atomic ensembles. *Nature* **438**, 828–832 (2005).
34. Chanelière, T. et al. Storage and retrieval of single photons transmitted between remote quantum memories. *Nature* **438**, 833–836 (2005).
35. Jing, B. et al. Entanglement of three quantum memories via interference of three single photons. *Nat. Photonics* **13**, 210–213 (2019).
36. van der Wal, C. H. et al. Atomic memory for correlated photon states. *Science* **301**, 196–200 (2003).



37. Dou, J.-P. et al. A broadband DLCZ quantum memory in room-temperature atoms. *Commun. Phys.* **1**, 55 (2018).
38. Riedinger, R. et al. Non-classical correlations between single photons and phonons from a mechanical oscillator. *Nature* **530**, 313–316 (2016).
39. Riedinger, R. et al. Remote quantum entanglement between two micromechanical oscillators. *Nature* **556**, 473–477 (2018).
40. Lee, K. C. et al. Entangling macroscopic diamonds at room temperature. *Science* **334**, 1253–1256 (2011).
41. Laplane, C., Jobez, P., Etesse, J., Gisin, N. & Afzelius, M. Multimode and long-lived quantum correlations between photons and spins in a crystal. *Phys. Rev. Lett.* **118**, 210501 (2017).
42. Kutluer, K., Mazzer, M. & de Riedmatten, H. Solid-state source of nonclassical photon pairs with embedded multimode quantum memory. *Phys. Rev. Lett.* **118**, 210502 (2017).
43. Kutluer, K. et al. Time entanglement between a photon and a spin wave in a multimode solid-state quantum memory. *Phys. Rev. Lett.* **123**, 030501 (2019).
44. Zhong, M. et al. Optically addressable nuclear spins in a solid with a six-hour coherence time. *Nature* **517**, 177 (2015).
45. Ma, Y., Ma, Y.-Z., Zhou, Z.-Q., Li, C.-F. & Guo, G.-C. One-hour coherent optical storage in an atomic frequency comb memory. *Nat. Commun.* **12**, 2381 (2021).
46. Raymer, M. G., Walmsley, I. A., Mostowski, J. & Sobolewska, B. Quantum-theory of spatial and temporal coherence properties of stimulated Raman-scattering. *Phys. Rev. A* **32**, 332–344 (1985).
47. Jiang, L., Taylor, J. M. & Lukin, M. D. Fast and robust approach to long-distance quantum communication with atomic ensembles. *Phys. Rev. A* **76**, 012301 (2007).
48. Simon, C. et al. Quantum repeaters with photon pair sources and multimode memories. *Phys. Rev. Lett.* **98**, 190503 (2007).
49. Stuart, J. S., Hedges, M., Ahlefeldt, R. & Sellars, M. Initialization protocol for efficient quantum memories using resolved hyperfine structure. *Phys. Rev. Res.* **3**, L032054 (2021).
50. Reddy, D. V., Nerem, R. R., Nam, S. W., Mirin, R. P. & Verma, V. B. Superconducting nanowire single-photon detectors with 98% system detection efficiency at 1550 nm. *Optica* **7**, 1649–1653 (2020).
51. Lita, A. E., Miller, A. J. & Nam, S. W. Counting near-infrared single-photons with 95% efficiency. *Opt. Express* **16**, 3032–3040 (2008).
52. Divochiy, A. et al. Superconducting nanowire photon-number-resolving detector at telecommunication wavelengths. *Nat. Photonics* **2**, 302 (2008).
53. Rancic, M., Hedges, M. P., Ahlefeldt, R. L. & Sellars, M. J. Coherence time of over a second in a telecom-compatible quantum memory storage material. *Nat. Phys.* **14**, 50–54 (2018).
54. Li, P.-Y. et al. Hyperfine structure and coherent dynamics of rare-earth spins explored with electron-nuclear double resonance at subkelvin temperatures. *Phys. Rev. Appl.* **13**, 024080 (2020).
55. Mehring, M., Mende, J. & Scherer, W. Entanglement between an electron and a nuclear spin 1/2. *Phys. Rev. Lett.* **90**, 153001 (2003).
56. Morton, J. J. L. et al. Solid-state quantum memory using the p-31 nuclear spin. *Nature* **455**, 1085–1088 (2008).
57. Simmons, S. et al. Entanglement in a solid-state spin ensemble. *Nature* **470**, 69–72 (2011).
58. Mehring, M., Scherer, W. & Weidinger, A. Pseudoentanglement of spin states in the multilevel  $^{15}\text{N}@C_{60}$  system. *Phys. Rev. Lett.* **93**, 206603 (2004).
59. Scherer, W. & Mehring, M. Entangled electron and nuclear spin states in  $^{15}\text{N}@C_{60}$ : density matrix tomography. *J. Chem. Phys.* **128**, 052305 (2008).
60. Wang, Y. et al. Preservation of bipartite pseudoentanglement in solids using dynamical decoupling. *Phys. Rev. Lett.* **106**, 040501 (2011).
61. Dehollain, J. P. et al. Bell's inequality violation with spins in silicon. *Nat. Nanotechnol.* **11**, 242–246 (2016).
62. Steffen, M. et al. Measurement of the entanglement of two superconducting qubits via state tomography. *Science* **313**, 1423–1425 (2006).
63. Filipp, S. et al. Two-qubit state tomography using a joint dispersive readout. *Phys. Rev. Lett.* **102**, 200402 (2009).
64. Aharonov, Y. & Anandan, J. Phase-change during a cyclic quantum evolution. *Phys. Rev. Lett.* **58**, 1593–1596 (1987).
65. Suter, D., Mueller, K. T. & Pines, A. Study of the Aharonov-Anandan quantum phase by NMR interferometry. *Phys. Rev. Lett.* **60**, 1218–1220 (1988).
66. Levitt, M. H. Composite pulses. *Prog. Nucl. Mag. Res. Sp.* **18**, 61–122 (1986).
67. Wesenberg, J. & Mølmer, K. Robust quantum gates and a bus architecture for quantum computing with rare-earth-ion-doped crystals. *Phys. Rev. A* **68**, 012320 (2003).
68. Morton, J. J. L. et al. High fidelity single qubit operations using pulsed electron paramagnetic resonance. *Phys. Rev. Lett.* **95**, 200501 (2005).
69. Sangouard, N., Simon, C., Coudreau, T. & Gisin, N. Purification of single-photon entanglement with linear optics. *Phys. Rev. A* **78**, 050301 (2008).
70. Li, C., Wyon, C. & Moncorge, R. Spectroscopic properties and fluorescence dynamics of  $\text{Er}^{3+}$  and  $\text{Yb}^{3+}$  in  $\text{Y}_2\text{SiO}_5$ . *Ieee J. Quantum Elect.* **28**, 1209–1221 (1992).

## Acknowledgements

This work is supported by the National Key R&D Program of China (No. 2017YFA0304100), the National Natural Science Foundation of China (Nos. 11774331, 11774335, 11504362, 11821404, and 11654002), the Fundamental Research Funds for the Central Universities (No. WK2470000026 and No. WK2470000029), and China Post-doctoral Science Foundation (No. 2021M703105). Z.-Q.Z. acknowledges the support from the Youth Innovation Promotion Association CAS.

## Author contributions

C.L., T.T., and Z.-Q.Z. carried out the theory, Z.-Q.Z. designed the experiment. C.L. and P.-Y.L. performed the experiment assisted by X.L., T.T., C.L., and X.-Y.Z. analyzed the experimental results. Z.-Q.Z., C.-F.L., and G.-C.G. supervised the project. C.L. and T.T. wrote the paper with input from other authors. All authors discussed the theory, experimental procedures and results.

## Competing interests

The authors declare no competing interests.

## Additional information


**Supplementary information** The online version contains supplementary material available at <https://doi.org/10.1038/s42005-022-00835-0>.

**Correspondence** and requests for materials should be addressed to Tao Tu, Zong-Quan Zhou or Chuan-Feng Li.

**Peer review information** *Communications Physics* thanks the anonymous reviewers for their contribution to the peer review of this work. Peer reviewer reports are available.

**Reprints and permission information** is available at <http://www.nature.com/reprints>

**Publisher's note** Springer Nature remains neutral with regard to jurisdictional claims in published maps and institutional affiliations.

 **Open Access** This article is licensed under a Creative Commons Attribution 4.0 International License, which permits use, sharing, adaptation, distribution and reproduction in any medium or format, as long as you give appropriate credit to the original author(s) and the source, provide a link to the Creative Commons license, and indicate if changes were made. The images or other third party material in this article are included in the article's Creative Commons license, unless indicated otherwise in a credit line to the material. If material is not included in the article's Creative Commons license and your intended use is not permitted by statutory regulation or exceeds the permitted use, you will need to obtain permission directly from the copyright holder. To view a copy of this license, visit <http://creativecommons.org/licenses/by/4.0/>.

© The Author(s) 2022